ISPRS Journal of Photogrammetry and Remote Sensing 109 (2015) 1–16

Contents lists available at ScienceDirect

ISPRS Journal of Photogrammetry and Remote Sensing

journal homepage: www.elsevier.com/locate/isprsjprs

# Forest cover maps of China in 2010 from multiple approaches and data sources: PALSAR, Landsat, MODIS, FRA, and NFI

Yuanwei Qin[a], Xiangming Xiao[a,b,*], Jinwei Dong[a], Geli Zhang[a], Masanobu Shimada[c], Jiyuan Liu[d], Chungan Li[e], Weili Kou[f], Berrien Moore III[g]

[a] Department of Microbiology and Plant Biology, Center for Spatial Analysis, University of Oklahoma, Norman, OK 73019, USA
[b] Institute of Biodiversity Science, Fudan University, Shanghai 200433, China
[c] Japan Aerospace Exploration Agency, Earth Observation Research Center, Sengen 2-2-1, Tsukuba, Ibaraki 305-8505, Japan
[d] Institute of Geographic Sciences and Natural Resources Research, Chinese Academy of Sciences, Beijing 100101, China
[e] Guangxi Forest Inventory and Planning Institute, Nanning, Guangxi 530000, China
[f] Southwest Forestry University, Kunming, Yunnan 650224, China
[g] College of Atmospheric and Geographic Science, University of Oklahoma, Norman, OK 73019, USA

A R T I C L E  I N F O

*Article history:*
Received 9 March 2015
Received in revised form 19 June 2015
Accepted 27 August 2015

*Keywords:*
Forest
PALSAR
MODIS
FRA
NLCD
China

A B S T R A C T

Forests and their changes are important to the regional and global carbon cycle, biodiversity and ecosystem services. Some uncertainty about forest cover area in China calls for an accurate and updated forest cover map. In this study, we combined ALOS PALSAR orthorectified 50-m mosaic images (FBD mode with HH and HV polarization) and MODIS time series data in 2010 to map forests in China. We used MODIS-based NDVI dataset (MOD13Q1, 250-m spatial resolution) to generate a map of annual maximum NDVI and used it to mask out built-up lands, barren lands, and sparsely vegetated lands. We developed a decision tree classification algorithm to identify forest and non-forest land cover, based on the signature analysis of PALSAR backscatter coefficient data. The PALSAR-based algorithm was then applied to produce a forest cover map in China in 2010. The resulting forest/non-forest classification map has an overall accuracy of 96.2% and a Kappa Coefficient of 0.91. The resultant 50-m PALSAR-based forest cover map was compared to five forest cover databases. The total forest area ($2.02 \times 10^6$ km$^2$) in China from the PALSAR-based forest map is close to the forest area estimates from China National Forestry Inventory ($1.95 \times 10^6$ km$^2$), JAXA ($2.00 \times 10^6$ km$^2$), and FAO FRA ($2.07 \times 10^6$ km$^2$). There are good linear relationships between the PALSAR-based forest map and the forest maps from the JAXA, MCD12Q1, and NLCD-China datasets at the province and county scales. All the forest maps have similar spatial distributions of forest/non-forest at pixel scale. Our PALSAR-based forest map recognizes well the agro-forests in China. The results of this study demonstrate the potential of integrating PALSAR and MODIS images to map forests in large areas. The resultant map of forest cover in China in 2010 can be used for many studies such as forest carbon cycle and ecological restoration.


## 1. Introduction

Forest areas are estimated to be $4.0 \times 10^7$ km$^2$, accounting for ~31% of the world land area (FAOSTAT, 2011). Forests produce half of net primary production in the world (Groombridge and Jenkins, 2002), and play an important role in the global carbon cycle (Bonan, 2008; Fang et al., 2014b; Pan et al., 2011; Yu et al., 2014), water and heat fluxes (Pongratz et al., 2010), biodiversity, and soil and water conservation (Achard and Hansen, 2012). In history, about 40% of global forests have been converted to cropland, pasture, and other man-made land cover types, especially for the Mediterranean forests, and temperature deciduous and dry tropical forests, in response to increasing demand for food, energy, and economic interests (Achard and Hansen, 2012; Foley et al., 2005). In the last several decades, more than 80% of the world agricultural expansion occurred in the tropical forest regions (Gibbs et al., 2010). In the future, the increasing population and the improvement of people's living conditions will continue to create significant demand and pressure on forests (FAO, 2009). Forests are also affected by other disturbances, including wild fires,

* Corresponding author at: Center for Spatial Analysis, University of Oklahoma, USA.
*E-mail address:* xiangming.xiao@ou.edu (X. Xiao).

http://dx.doi.org/10.1016/j.isprsjprs.2015.08.010
0924-2716/

freezing rain, drought, and insect pests. The loss and degradation of forests could affect various ecosystem services and result in a series of ecological disasters. To reverse the adverse effects from deforestation and forest degradation, extensive reforestation and afforestation activities have also been carried out in many parts of the world over the last several decades, especially in East Asian countries, such as the "Grain for Green" project in China and reforestation projects in Vietnam (FAO, 2012; Lambin and Meyfroidt, 2011; Liu et al., 2014; Xiao, 2014). These reforestation and afforestation mainly occurred in the abandoned or marginal lands, which increases the forest area and carbon sequestration (Fang et al., 2014b; Lambin and Meyfroidt, 2011). Timely and accurate forest cover monitoring algorithm and data products are needed for forest management (Hansen et al., 2008).

Optical images from airborne and space-borne sensors have been used for monitoring forest areas and assessing forest cover change (Potapov et al., 2011). The coarse spatial resolution images from high-revisit-cycle satellites (e.g., National Oceanic and Atmospheric Administration (NOAA)-Advanced Very High Resolution Radiometer (AVHRR), SPOT4 VEGETATION, Moderate Resolution Imaging Spectroradiometer (MODIS)) were used for global and regional land cover mapping (e.g., forests), such as IGBP DIScover (Loveland et al., 2000), UMd land cover dataset from the University of Maryland (Hansen et al., 2000), GLC2000 (Bartholome and Belward, 2005), GlobCover (Bontemps et al., 2011), and MCD12Q1 (Friedl et al., 2010). The updated global MCD12Q1 land cover maps are available at 500-m spatial resolution annually, and have been used to identify land cover changes since 2000 (Friedl et al., 2010). Considering the uncertainties caused by mixed pixels from the coarse spatial resolution, there is a need for using fine spatial resolution images to map forest distribution and their inter-annual changes. The freely-available Landsat archive with more than 30 years of global observation records provides a valuable resource for mapping forests at 30-m spatial resolution. Giri et al. (2011) interpreted approximately 1000 Landsat scenes to map the spatial distribution of world mangrove forest, using hybrid supervised and unsupervised classification. Gong et al. (2013) produced the first 30-m resolution global land cover maps using Landsat TM/ETM+ images mainly from circa 1999 and circa 2011. Hansen et al. (2013) generated 30-m global forest cover change maps based on Landsat images from circa 2000 and circa 2012.

Synthetic Aperture Radar (SAR) sensors with different bandwidths (X, C and L bands) can penetrate clouds, and provide another source of images to map forests. The L-band microwave energy has greater penetration into forests and exhibits substantial volume scattering, as incident energy interacts with a large number of leaves, trunks, and branches, and thus is preferred for global and regional forest mapping. The Japanese Earth Resources Satellite-1 (JERS-1) was the first L-band SAR with HH polarization and used for global forest analysis and mapping (Rosenqvist et al., 2000; Shimada, 2005). Shimada et al. (2014) generated the first 25-m global forest maps from 2007 to 2010, using region-specific threshold values of Phased Array type L-band Synthetic Aperture Radar (PALSAR) HV backscatter coefficients as forest and non-forest have larger differences in HV gamma naught than those in HH. In some hotspots, the potential of PALSAR Fine Beam Dual (FBD) mode images was assessed for mapping deforestation in tropical (Longepe et al., 2011; Motohka et al., 2014; Rakwatin et al., 2012) and boreal (Pantze et al., 2014) regions. However, forest mapping results based on only SAR data would have some noise that is introduced by soil moisture and complex environment.

The combination of optical and SAR images provides complementary information and often increases the classification accuracy of land covers (Ban et al., 2010; Leinenkugel et al., 2011). High quality and time-specific optical images (e.g., ALOS AVNIR-2, Landsat, and MODIS) have been combined with PALSAR FBD data to identify and monitor local land cover types (e.g., forests) (Bagan et al., 2012; Dong et al., 2013, 2012b; Hoan et al., 2013; Lehmann et al., 2012), or large area of forests at 500-m spatial resolution (Sheldon et al., 2012). Most of these studies were carried out at local hot spots in tropical regions, and highlight the potential of combining PALSAR and optical data for mapping forests.

In this study, we aim to map forests through integration of PALSAR and MODIS images acquired in 2010. The Chinese government has successively implemented several ecological restoration projects that aim to convert and improve the deteriorated ecological conditions with huge investment and labor force, including reforestation and afforestation (Fang et al., 2001; FAO, 2012). It was reported that forest area in Asia shifted from net loss during 1990–2000 to great net gain during 2000–2010, mainly due to the afforestation in China (FAO, 2012). However, a recent study indicated that there was no obvious forest area increase in China during 2000–2012 (Hansen et al., 2013). Because of the large uncertainty of forest area estimates among available multi-source forest products, it is necessary to develop an accurate forest distribution map at fine (e.g., 50-m) spatial resolutions and estimate forest area. The objectives of this study are (1) to develop an algorithm to generate an accurate 50-m forest map in China in 2010, combining the PALSAR FBD data with MOD13Q1 NDVI; (2) to compare multi-source forest maps and quantify their agreement and disagreement; and (3) to investigate the uncertainties of multi-source forest maps in China in 2010. This study could provide a high quality forest map in China for various scientific research, forest planning and management.

## 2. Materials and methods

### 2.1. Study area

China is situated in East Asia, and climate has distinct regional and seasonal characteristics due to East Asian Monsoon and complex topography (Fig. S1). The southeast marine monsoon prevails from May to September and brings a large amount of rainfall, while the northwest continental monsoon occurs from November to March and brings dry and cool air. Southeast China has a warm and humid climate, while Northwest China has a dry and cool climate. The Tibetan Plateau is characterized by cold and dry climate because of the massive mountain ranges with high elevation.

The topography varies greatly from Eastern to Western China, with an elevation range of −156 m to 8685 m above sea level (Fig. S1). The Tibetan Plateau has an average elevation approximately 4500 m above sea level, followed by the plateaus and mountains in Mid-western China (with an average elevation about 1000–3000 m) and the plains and hills in coastal areas (mostly lower than 500 m). The mountain area is about 2/3 of the total area in the country. The major agricultural production regions are located in the plains and basins. Grassland (31.0% of the total land area), woodland (24.8%), unused land (23.2%), and cropland (15.6%) are the major land cover types in China in 2010, while water bodies and built-up land account for 2.9% and 2.5%, respectively (Zhang, 2012).

### 2.2. 50-m PALSAR orthorectified mosaic dataset and pre-processing

The 50-m PALSAR orthorectified mosaic data with FBD polarization mode from 2007 to 2010, aggregated from the original observation with minimum response to surface moisture (Shimada et al., 2014), is available on the Earth Observation Research Center, Japan Aerospace Exploration Agency (JAXA). The dataset is organized in latitude–longitude coordinate, and each tile has 2250 columns by 2250 rows. The dataset includes gamma-naught in HH and HV, local incidence angle and mask information (layover, shadowing, ocean flag, effective flag and void flag), and total dates since the ALOS launch. The HH and HV data are slope corrected and orthorectified using the 90-m Shuttle Radar Topography Mission (SRTM) Digital Elevation Model (DEM), and radiometrically calibrated. Because of the coarse spatial resolution of SRTM DEM, the geometric accuracy of PALSAR HH and HV is about 12-m. Gamma naught is normalized by the realistic illumination area using the local incidence angle, and provides more uniform backscattering coefficients than sigma naught (Shimada et al., 2014; Shimada and Ohtaki, 2010). The Digital Number (DN) values (amplitude values) in the data were converted into gamma-naught in decibel units using a calibration coefficient, which is insensitive to the focus of the impulse response (Shimada et al., 2009). Then we calculated the Ratio and Difference values, using the resultant HH and HV backscattering coefficient in decibel.

$$\gamma^{\circ} = 10 \times log_{10} < \mathrm{DN}^2 > + \mathrm{CF}$$

where $\gamma^{\circ}$ is the backscattering coefficient in decibel; DN is the digital number value of pixels in HH or HV; and CF is the absolute calibration factor of $-83$, which is dependent on incidence-angle (Shimada et al., 2009) and can be used for the radiometric calibration of both sigma-naught and gamma-naught.

$$\mathrm{Ratio} = \gamma^0_{HH}/\gamma^0_{HV}$$

$$\mathrm{Difference} = \gamma^0_{HH} - \gamma^0_{HV}$$

where Ratio and Difference are the ratio values of $\gamma^0_{HH}$ to $\gamma^0_{HV}$ and the difference values of $\gamma^0_{HH} - \gamma^0_{HV}$, respectively; $\gamma^0_{HH}$ and $\gamma^0_{HV}$ are the backscattering coefficients of HH and HV in decibel.

We downloaded all the PALSAR HH and HV data in China in 2010 and converted to backscattering coefficient in decibel (Fig. 1). To reduce the adverse effects of snow, ice and soil moisture, we selected the PALSAR data in the main growing season according to the climate zones (Fig. S2). One strip in the boreal zone in Northeastern China was acquired in October, 2010, which was out of growing season, and then replaced by the PALSAR data acquired in September, 2009.

### 2.3. MODIS NDVI dataset for a mask of barren land, built-up land and sparse vegetation

Some built-up lands, barren lands, and sparsely vegetated lands with complex structure and rough land surface may have high PALSAR backscattering coefficients, similar to forests. The annual maximum NDVI ($NDVI_{max}$) of these built-up lands, barren lands, and sparsely vegetated lands are usually lower than 0.3, while forests $NDVI_{max}$ are usually higher than 0.5 (Defries and Townshend, 1994). To reduce the commission error, we generated a map of barren land, built-up and sparsely vegetation, based on the threshold value of $NDVI_{max} < 0.5$ from 16-day composite MOD13Q1 NDVI product (250-m spatial resolution) in 2010 (Solano et al., 2010) (Fig. 2). The resultant map of barren land, built-up land and sparse vegetation was applied as a mask to the data analysis of PALSAR images.

### 2.4. PALSAR-based forest mapping algorithm

According to the FAO, forest is defined as land with tree canopy cover larger than 10% with a minimum height of five meters (FAO, 2012) in this study. In the previous PALSAR-based forest mapping studies (Dong et al., 2012a; Sheldon et al., 2012; Shimada et al., 2014), the same forest definition was used. A detailed workflow is developed for forest mapping and multi-source forest dataset comparison (Fig. 3). L-band PALSAR data can capture the structure and above ground biomass (AGB) of forests (Imhoff, 1995; Kovacs

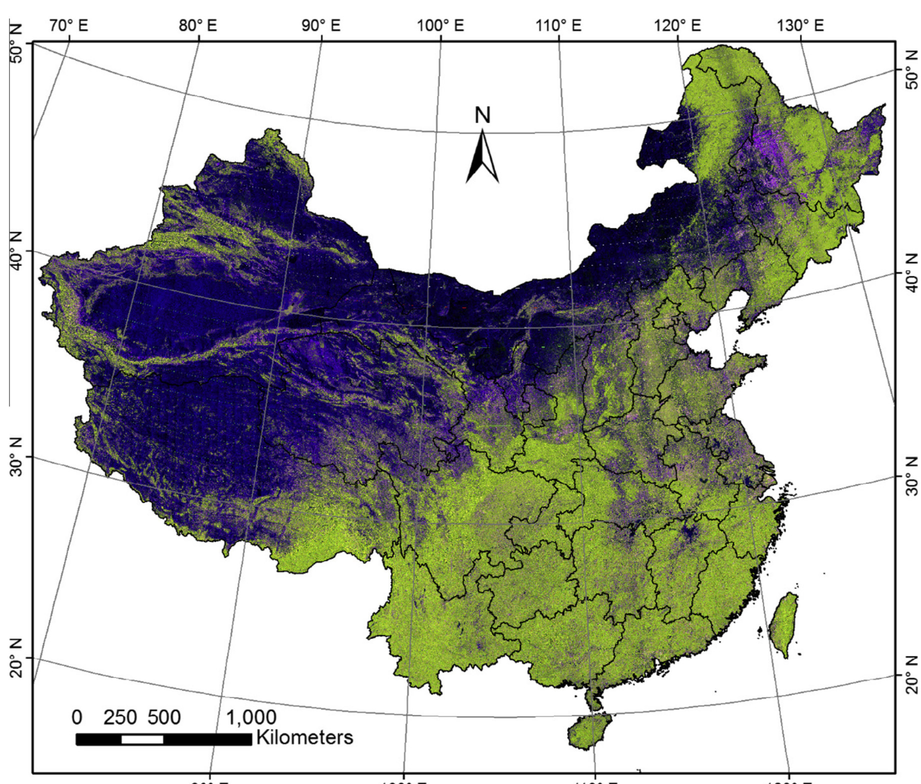


**Fig. 1.** Color composite map of PALSAR images at the spatial resolution of 50 m in China for 2010, in a false-color combination of Red (HH), Green (HV), and Blue (Difference). (For interpretation of the references to color in this figure legend, the reader is referred to the web version of this article.)

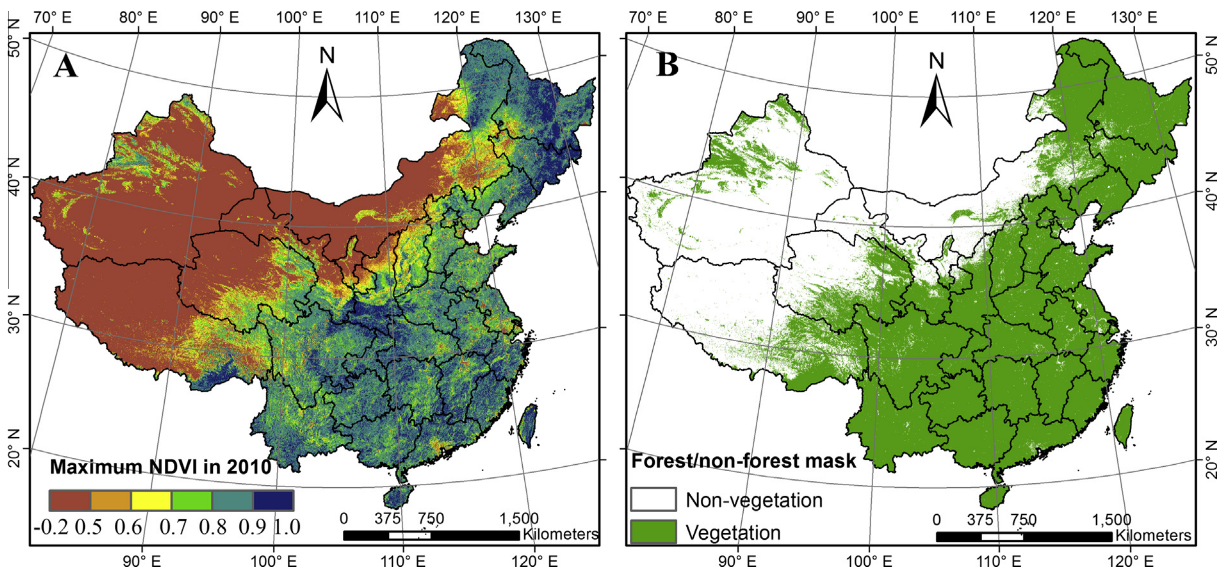


**Fig. 2.** Spatial distribution of annual maximum NDVI (A) and the binary map of vegetation/non-vegetation mask (B), based on 16-day MOD13Q1 NDVI in China in 2010.

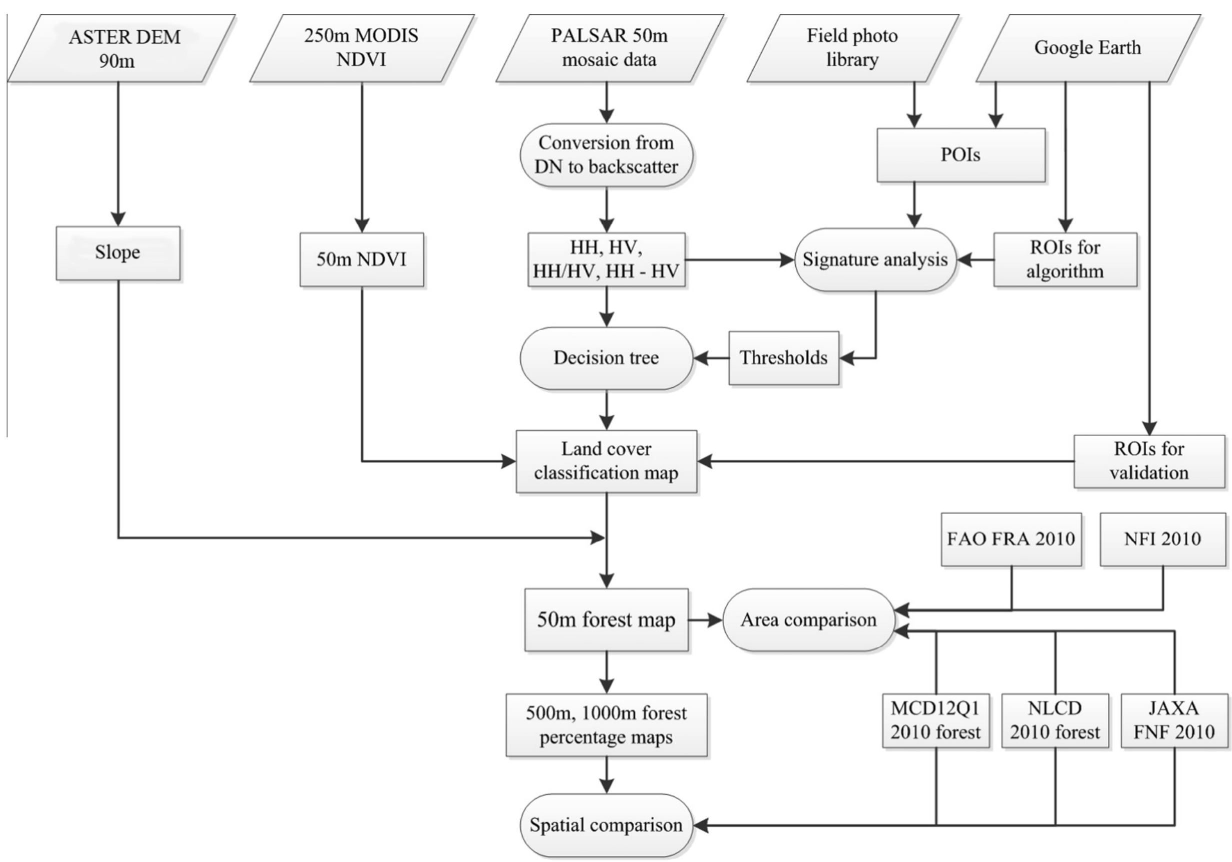


**Fig. 3.** Workflow of forest cover mapping based on PALSAR and MODIS products in China.

et al., 2013; Ni et al., 2013), as its great penetration into forests with substantial volume scattering through the incident energy interaction with large trunks and branch components. Forests usually have dense and large canopy and relative high AGB from tremendous number of leaves, branches, stems, and trunks. Recent studies show that forests and forest AGB exhibit a certain range of PALSAR backscattering coefficients, respectively (Ni et al., 2013; Peregon and Yamagata, 2013; Rakwatin et al., 2012; Shimada et al., 2014). In this study, we tried to use the same decision classification algorithm in our previous study in Southeast Asia (Dong et al., 2012a, 2014). As the backscatter data used in this study is gamma naught instead of sigma naught, we recalculated the segmentation thresholds by using the same training samples.

Ground truth samples are important for land cover classification, which are used for training or result validation. A total of 2106 geo-referenced field photos are used for algorithm development in this study, which were collected in Mainland Southeast Asia in 2009 and are freely available in Global Geo-referenced Field Photo Library (http://www.eomf.ou.edu/photos/). We located those geo-referenced photos in Google Earth, and digitalized a series of random Region of Interests (ROIs) as a reference of geo-referenced photos and high spatial resolution images. About $1.4 \times 10^7$ PALSAR pixels were acquired from the ROIs, including $9.98 \times 10^5$ forest pixels (25 ROIs), $1.61 \times 10^5$ cropland pixels (32 ROIs), $3.04 \times 10^5$ water pixels (10 ROIs), and $2.70 \times 10^4$ built-up pixels (11 ROIs) (Dong et al., 2012a). These ROIs were used for PALSAR backscatter signature analysis and classification thresholds among different land cover types (water, cropland, built-up, and forests) (Fig. 4).

We calculated and generated the frequency distribution of two polarizations (HH and HV), Ratio, and Difference of forests, cropland, water, and built-up lands. The histogram of the HH image (Fig. 4A) shows that water has much lower backscatter values than forests and partly overlapped with cropland, as water bodies are calm and smooth, and can reflect most of the backscatter through specular reflection. Water is separable from forests, built-up lands, and most of cropland in HH backscatter. Both forests and built-up lands have high HH backscatter values due to the strong reflectance environment caused by their complex structure, and parts of built-up lands have even higher HH backscatter values. Forests, cropland, and built-up lands also have some overlap of HH backscatter values. The histogram of the HV image (Fig. 4B) shows that forests present higher values than water and cropland, and have relatively more overlap with built-up lands due to the mixed pixels of forests and build-up lands. HV is an additional and effective indicator to distinguish forests from water and cropland, and is still limited to distinguish forests and built-up lands. The histogram of the Ratio image (Fig. 4C) shows that forests overlap with the other three land cover types. The histogram of the Difference image (Fig. 4D) shows that forests have low difference values, while water has high Difference values.

The backscatter signatures of HH, HV, Ratio, and Difference are the basis to build the decision tree algorithm to identify forests, cropland, water, and built-up lands. First, water can be identified easily as it has very low HH and HV values. Second, forests have high HH and HV values, and low Difference values, although it partly overlaps with built-up lands. Third, most of cropland can also be identified, although partly overlap with water. Based on the 95% confidence intervals of the HH, HV, Ratio, and Difference images, threshold values for the decision tree algorithm are determined (Fig. 5). As some uncertainty may exist in the ROIs of different land cover types, we exclude 2.5% pixels with the lowest and highest values. The threshold values were further rounded to integer numbers for HH and HV images, and to 0.5 for Ratio and Difference images.

The PALSAR-based land cover mapping results were merged into forest and non-forest. Through a dynamic link between the forest/non-forest map and high spatial resolution images in Google Earth, some noise was found, which may be attributed to the complex topography, soil moisture, etc. Based on the slope distribution map (Fig. S3) derived from the 90-m STRM DEM, we used 3 pixels by 3 pixels median filter to exclude those noise in the area with slope larger than 5°. In addition, the spatial distribution of $NDVI_{max}$ (Fig. 2B) was used to further reduce the commission errors in the forest/non-forest map, caused by some built-up lands and bare lands that have large values of backscattering coefficients. After these two post-processing refinements, we got the final forest/non-forest map derived from PALSAR/MODIS, named OU F/NF map.

### 2.5. ROIs for results validation and threshold values comparison

We set up the grid of one latitude degree by one longitude degree in China (1127 grid cells). Based on high spatial resolution images available in Google Earth in circa 2010, we manually digitalized ROIs through visual interpretation across the country in each of 1° by 1° grid cells (Fig. 6). The high spatial resolution images during the growing season were collected, and the land covers can be clearly identified. Finally, 362,976 pixels (2120 ROIs) were selected, including 98,820 pixels of forests (1520 ROIs) and 264,156 pixels of non-forests (600 ROIs). These ROIs were used to compare threshold values for forests between Mainland

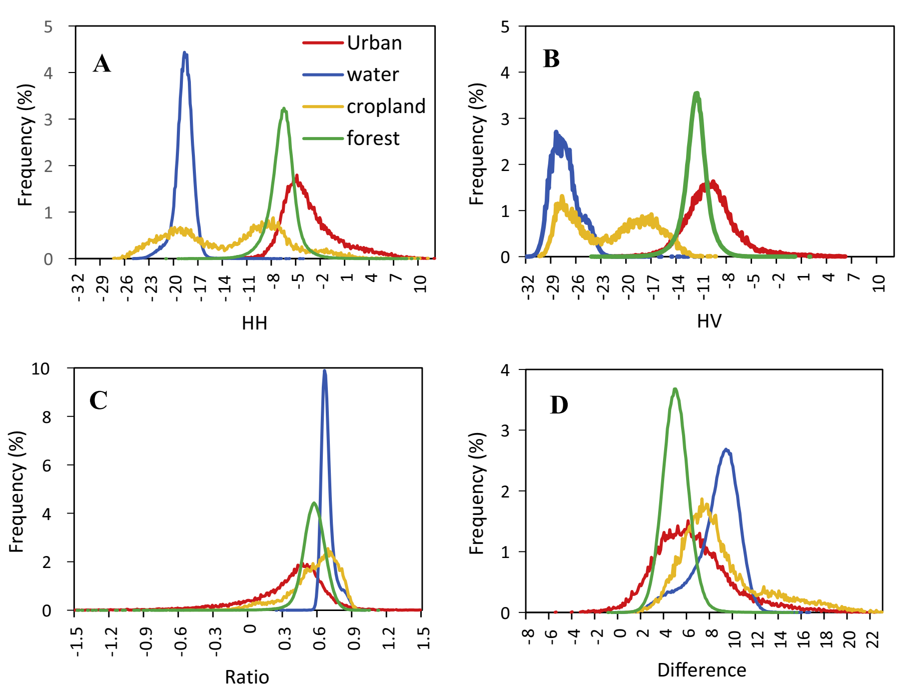


**Fig. 4.** The backscatter signature of different land cover types based on ALOS PALSAR FBD gamma naught.

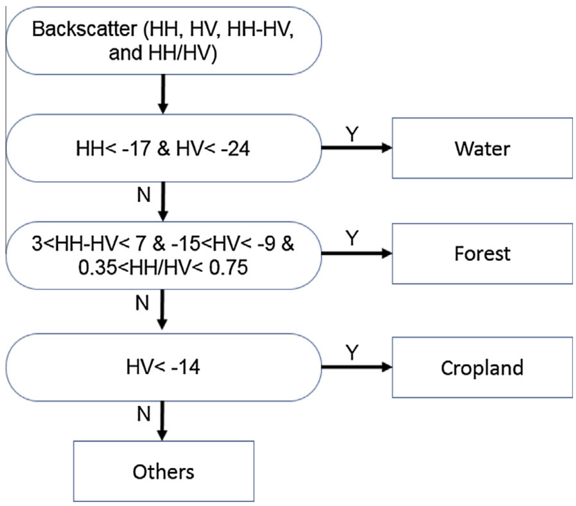


**Fig. 5.** Decision tree classification for forest mapping based on PALSAR backscatter in China.

Southeast Asia (Dong et al., 2012a) and China, and to validate the accuracy of forest/non-forest mapping result in this study.

*2.6. Comparison with multi-source forest datasets in 2010*

We collected three remote sensing-based forest datasets and two inventory-based forest datasets available in the public domain. We first compared the area and spatial distribution of these six forest datasets in China in 2010 at country, province, and county scales, respectively. For the spatial comparison, the 50-m OU F/NF and JAXA F/NF maps and 500-m MCD12Q1 F/NF map were aggregated into 1000-m. Here we provide a brief introduction of these five datasets for inter-comparison (Table 1).

*2.6.1. JAXA forest/non-forest map (JAXA F/NF)*

The 50-m JAXA F/NF maps were aggregated from the original 25-m F/NF maps, which were produced by using PALSAR FBD mode data from June to September (Shimada et al., 2014). About 10–15% of the data in the year before or after were used due to the data availability. Data pre-processing includes speckle reduction, ortho-rectification and slope correction, and intensity equalization between neighboring strips. In general, three steps were used to generate the JAXA F/NF maps. First, a $5 \times 5$ pixel median filter was used to reduce noise in images, following a multi-resolution segmentation in eCognition software. Then, 15 region-specific HV threshold values were determined to identify forest pixels, based on the ROIs and cumulative distribution functions. Finally, the overall accuracy of JAXA F/NF maps were assessed approximately 85%, 91% and 95%, using validation points from the Degree Confluence Projects, forest area statistics from Global Forest Resource Assessment, and Google Earth high spatial resolution images, respectively.

*2.6.2. MODIS land cover product (MCD12Q1)*

Five different land cover classification systems were included in the MCD12Q1 product (Friedl et al., 2010), and the International Geosphere-Biosphere Programme (IGBP) classification was used in this study. The IGBP classification map was produced using a supervised classification algorithm, based on the training dataset. The phenology and temporal variability features of land cover types extracted from 500-m aggregated 32-day average nadir BRDF-adjusted land surface reflectance (NBAR), enhanced vegetation index (EVI), land surface temperature (LST), and annual metrics (minimum, maximum, and mean values) for EVI, LST and NBAR bands were used to identify and generate land cover types. Post-processing refinements were applied to create the final land cover product, including sample bias correction and spatial explicit prior probability adjustments. The overall accuracy of the IGBP land cover product is about 75% based on a cross-validation. Five

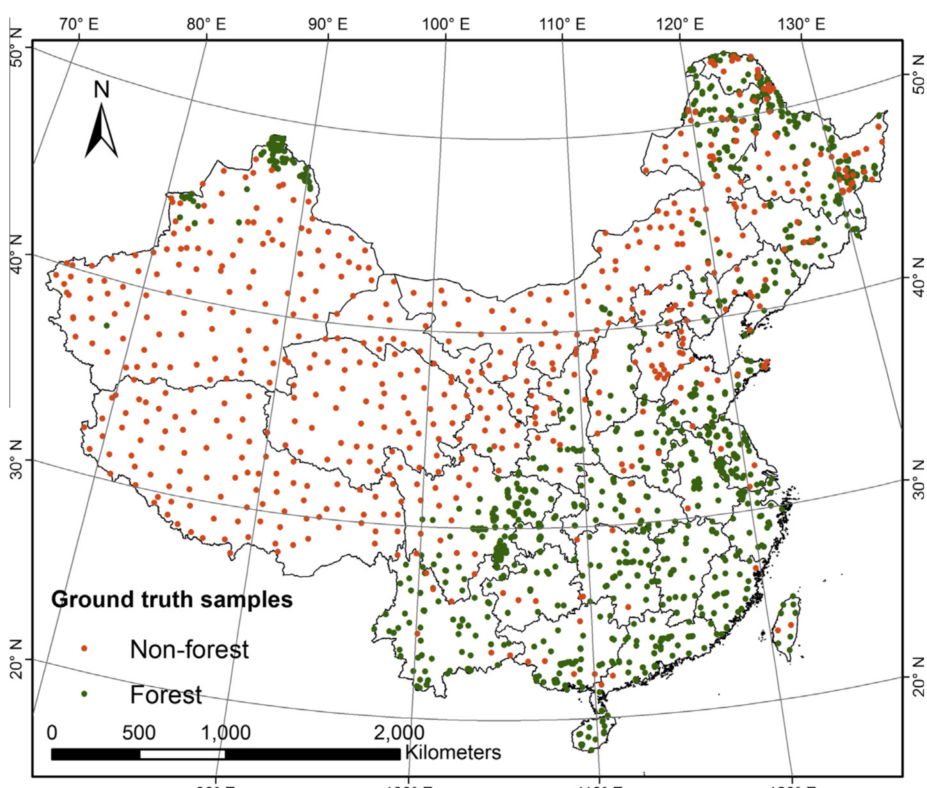


**Fig. 6.** Ground truth samples from high spatial resolution images in Google Earth in circa 2010.

**Table 1**
Multiple forest cover datasets used for comparison of forest cover area in China in 2010.

| Forest cover datasets | Forest land cover types | Spatial resolution (m) | Algorithms |
|---|---|---|---|
| MCD12Q1 (IGBP) | Woody vegetation with a percent cover more than 60% and tree height exceeding 2-m | 500-m | Supervised classification |
| NLCD-China | Wood canopy cover more than 10% | 1000-m (area percentage) | Visual interpretation and digitalization on the screen |
| JAXA F/NF | Woody vegetation cover more than 10%, determined by high spatial resolution images in Google Earth | 50-m (25-m original data) | Supervised classification |
| OU F/NF | Woody vegetation cover more than 10% and tree height exceeding 5-m, determined by high spatial resolution images in Google Earth | 50-m | Supervised classification |
| FAO FRA | Land spanning more than 0.5 ha with tree height exceeding 5-m and a canopy cover more than 10%, or trees able to reach these thresholds in situ | Country | Statistical datasets |
| NFI-China | Natural, secondary, and planted forests have more than 30% coverage | Country and province | Statistical datasets |

forest types in 2010 were merged into a forest mask, including evergreen needleleaf forest, evergreen broadleaf forest, deciduous needleleaf forest, deciduous broadleaf forest, and mixed forest.

*2.6.3. National Land Cover Dataset (NLCD-China)*

The NLCD-China dataset uses a hierarchical classification system, including 6 classes and 25 sub-classes (Liu et al., 2005). The main data sources for development of NLCD-China were 30-m Landsat TM/ETM+ images from the late 1980s to 2010. Most of the satellite images used were acquired in the vegetation growing season without cloud cover. Geometric correction was done for all the satellite images using ground control points, with the relative position error less than two pixels. Four steps were implemented in the NLCD-China classification projects (Zhang et al., 2014). First, interpretation symbols were built for the typical land use/cover types, according to the field survey. Second, the baseline NLCD-China for 1995 was produced. Interpreters analyzed and identified land use/cover types from Landsat TM images in 1994/1995, then digitalized the boundaries and labeled the properties for each polygon at the scale of 1:100,000. Third, interpreters compared the satellite images during different periods, and digitalized the Land use/cover changes (LULCC). Fourth, the NLCD-China in 1995 and the LULCC polygons from 1995 to 2010 were combined together to produce the NLCD-China in 2010. The vector data was intersected with a $1\,\text{km} \times 1\,\text{km}$ fishnet, and the area percentages of each land use/cover types were calculated as the values for each cell. NLCD-China was validated with a high accuracy of about 95% for the 6 classes, using the re-interpretation map of randomly 10% of counties and field survey photos.

*2.6.4. FAO Forestry Resources Assessments (FRA)*

FAO had a long history in monitoring the world-wide forests at 5–10 year intervals since 1946 (FAO, 2012). The previous FRA were mainly based on country reports collected from 233 countries and territories in 1990, 2000, 2005, and 2010. With the great development of remote sensing, satellite images became another important data source. FAO worked closely with countries and specialists in the design and implementation of FRA-2010. More than 900 contributors were involved, including 178 officially nominated national correspondents and their teams. FRA-2010 is the most comprehensive assessment of forests and forestry to date. It examines the current status and recent trends for about 90 variables covering the extent, condition, uses and values of forests. However, the data availability and quality are still limited, especially in developing countries.

*2.6.5. China National Forestry Inventory (NFI-China)*

To get the area, composition, and distribution of forest resources, the State Forestry Bureau of China organized eight National Forestry Inventories around 1975, 1980, 1985, 1990, 1995, 2000, 2005, and 2010, respectively (State Forestry Bureau, 2014). The survey samples were systematically allocated according to the principle of statistics. Based on the unified technical standard of continuous inventory method, investigators revisited the survey sample sites periodically, and processed the data and obtained the regional/national forest information using the statistical software. The overall accuracy of the results was assessed to be approximately 95% through the samplings (State Forestry Bureau, 2003). The forest area at the national and province scales from the eighth NFI-China (2010) was used in this study.

## 3. Results

*3.1. Forest map of China in 2010 from the 50-m PALSAR mosaic dataset (OU F/NF dataset)*

The resultant OU F/NF map estimates the forest area of approximately $2.02 \times 10^6\,\text{km}^2$ in 2010, which covers 21.31% of the land area in China. The spatial distribution of forests in China varies substantially over space (Figs. 7 and 8 and S1). About $1.7 \times 10^6\,\text{km}^2$ (85% of national forest area) forests are located in those areas with an elevation of under 2000 m, mainly in Northeastern and Southern China. About $3.0 \times 10^5\,\text{km}^2$ (15%) forests are detected in the grain production plain regions, such as Northeast China Plain, North China Plain, and Yangtze Plain with dense population and intensive agricultural production (Liu et al., 2005; Zhang et al., 2014). Only a small number of forests are in Western China, where there is a limitation for forests growing because of the dry and cold climate, and high elevation above sea level.

The ground truth samples from Google Earth were used to validate the classification accuracy of OU F/NF map. The OU F/NF map has an overall accuracy of 96.2% and a Kappa Coefficient of 0.9. The forest category has Producer Accuracy and User Accuracy of 87.6% and 98.1%, and non-forest category has Producer Accuracy and User Accuracy of 99.4% and 95.5% (Table 2). Forests in plain areas, with the elevation lower than 200 m, are also assessed with relative high accuracy through the ground truth samples in plain areas (Table 3). The omission error of forest is relatively higher than that of commission error. Spatial analysis of accuracy assessment shows that the omission error of the OU F/NF map is mainly located in cold regions in Northern China with short growing season and agricultural production regions with scattered forests (Figs. S1 and S4A). The omission and commission errors are ran-

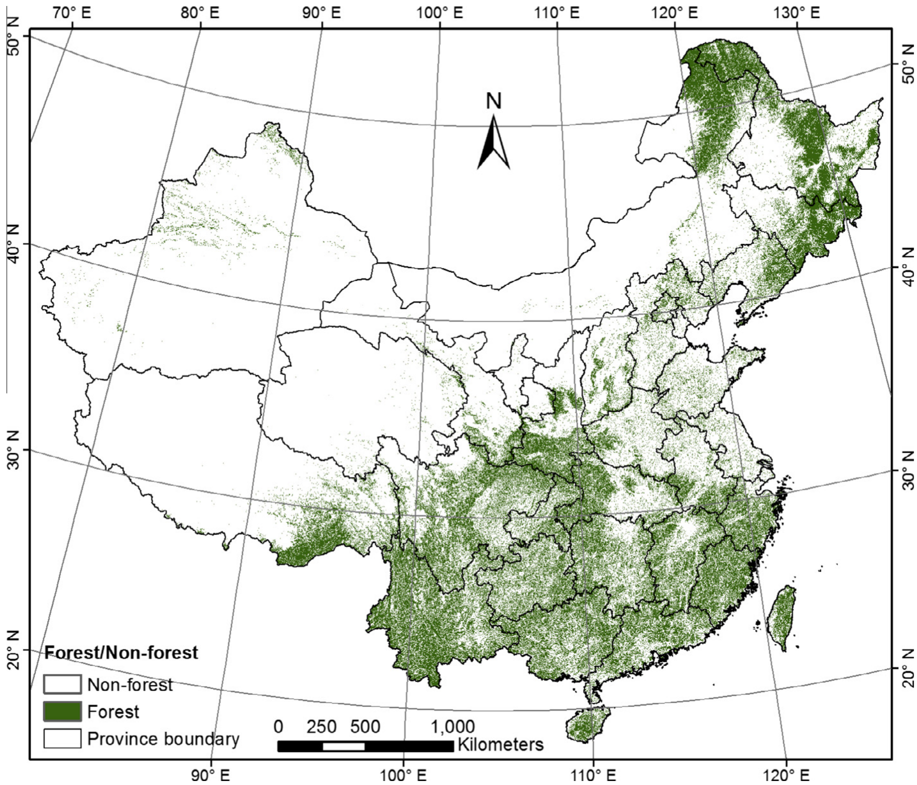


**Fig. 7.** Spatial distribution of 50-m OU forest/non-forest in China in 2010.

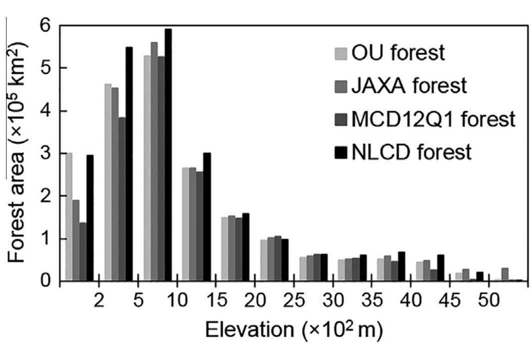


**Fig. 8.** Forest distribution in different elevation intervals at 1 km spatial resolution from multi-source forest maps in China in 2010.

domly distributed in the acquisition date of PALSAR datasets, elevation, local incidence angle, and terrain slope (Fig. S4B–E).

### 3.2. Area comparison of multi-source forest maps in 2010 at country, province and county levels

The total forest area of the OU F/NF map is quite close to those of NFI-China ($1.95 \times 10^6$ km$^2$), JAXA F/NF map ($2.00 \times 10^6$ km$^2$), and FAO FRA ($2.07 \times 10^6$ km$^2$), and has slightly larger differences with the MCD12Q1 ($1.74 \times 10^6$ km$^2$) and NLCD-China ($2.27 \times 10^6$ km$^2$) (Fig. 9). About 65% of forests are distributed in the area with elevation from 200 m to 1500 m in the multi-source forest maps (Fig. 8). The OU and NLCD-China F/NF maps identify more forests than the JAXA and MCD12Q1 F/NF maps in the flat area with elevation of lower than 200 m (Fig. 8).

Significant linear relationships exist among multi-source forest maps at province and county scales. At the province scale, the forest area of the OU F/NF map has significant linear relationships with those of JAXA ($R^2 = 0.98$, $p < 0.001$), MCD12Q1 ($R^2 = 0.96$, $p < 0.001$), NLCD-China ($R^2 = 0.93$, $p < 0.001$), and NFI-China ($R^2 = 0.82$, $p < 0.001$) F/NF maps with the Root Mean Squared Error (RMSE) about $0.88 \times 10^4$ km$^2$, $1.4 \times 10^4$ km$^2$, $1.8 \times 10^4$ km$^2$ and $2.5 \times 10^4$ km$^2$, respectively (Fig. 10). The slope of the forest area linear relationships between OU F/NF map and JAXA, MCD12Q1, NLCD-China, and NFI-China F/NF maps are about 1.02, 0.90, 1.09, and 1.02, respectively. At the county scale, the forest area of OU F/NF map has significant linear relationships with those of JAXA ($R^2 = 0.98$, $p < 0.001$), MCD12Q1 ($R^2 = 0.94$, $p < 0.001$), and NLCD-China ($R^2 = 0.95$, $p < 0.001$) F/NF maps, with the RMSE about $2.9 \times 10^2$ km$^2$, $4.5 \times 10^2$ km$^2$, $4.6 \times 10^2$ km$^2$, respectively (Fig. 11). The slope of the forest area linear relationships between

**Table 2**
Confusion matrix between OU F/NF map and ground truth samples from high spatial resolution images in Google Earth in 2010.

| | Class | Ground truth samples (pixels) | | Total classified pixels | User accuracy (%) |
|---|---|---|---|---|---|
| | | Forest | Non-forest | | |
| Classification | Forest | 86,571 | 1639 | 88,210 | 98.14 |
| | Non-forest | 12,249 | 262,517 | 274,766 | 95.54 |
| Total ground truth pixels | | 98,820 | 264,156 | 362,976 | |
| Producer accuracy (%) | | 87.60 | 99.38 | | |

**Table 3**
Confusion matrix in plain regions between OU F/NF map and ground truth samples from high spatial resolution images in Google Earth in 2010.

| | Class | Ground truth samples (pixels) | | Total classified pixels | User accuracy (%) |
|---|---|---|---|---|---|
| | | Forest | Non-forest | | |
| Classification | Forest | 11,522 | 486 | 12,008 | 95.95 |
| | Non-forest | 3003 | 77,553 | 80,556 | 96.27 |
| Total ground truth pixels | | 14,525 | 78,039 | 92,564 | |
| Producer accuracy (%) | | 79.33 | 99.38 | | |

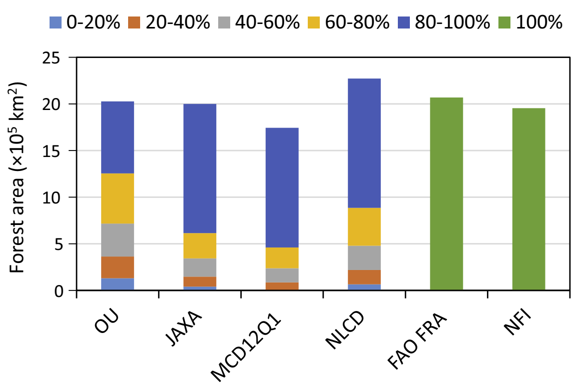


**Fig. 9.** Forest area comparison among multi-source forest maps in China in 2010.

OU F/NF and JAXA, MCD12Q1, and NLCD-China F/NF maps are about 1.06, 0.97, and 1.09, respectively.

### *3.3. Spatial comparison of multi-source forest cover datasets in 2010 at grid cell level*

The OU, JAXA, MCD12Q1, and NLCD-China F/NF maps present similar spatial distributions of forests at the spatial resolution of 1 km in China in 2010 (Fig. 12), although they were generated from different data source and algorithms. About 62% of the forest pixels have a forest area percentage below 80% in OU F/NF map, which is much higher than those of MCD12Q1 (26%), JAXA (31%), and NLCD-China (39%) F/NF maps (Fig. 9). The detailed comparisons of these forest maps are as followings.

There is a great agreement of forest/non-forest spatial distribution between the OU and JAXA F/NF maps. Approximately 83% of pixels have the forest area percentage deviation within the range of ±20% between the OU and JAXA F/NF maps at the same locations (Fig. 13A). Compared with JAXA F/NF map, OU F/NF map identified more forests in the major agriculture production plains with some scattered forests, and less forests in the mountain areas with complex reflectance environment in Northeastern China, Southern China, and Western China.

Approximately 78% of pixels have the forest area percentage deviation within the range of ±20% between the OU and MCD12Q1 F/NF maps (Fig. 13B). In the major agriculture production area and Western China, the OU F/NF map identifies more forests than the MCD12Q1 F/NF map, as the spatial resolution of MODIS data is a coarse (500-m) and not sensitive to the forests in small patch sizes. In the mountain areas, the OU F/NF map identifies a smaller amount of forests than the MCD12Q1 F/NF map. Some relatively large differences between the OU and MCD12Q1 F/NF maps occurred in Southwestern China.

Approximately 78% of pixels have the forest area percentage deviation within the range of ±20% between OU and NLCD-China F/NF maps (Fig. 13C). The NLCD-China is easy to omit small patches of forests and include small areas of other land cover types into large areas of forests through visual interpretation (Liu et al., 2005), and the OU F/NF map has some random omission and commission errors (Fig. S4). The OU F/NF map has more forests in the major agriculture production area, and Central and Northwestern China, but less area of forests in mountain regions in Southern

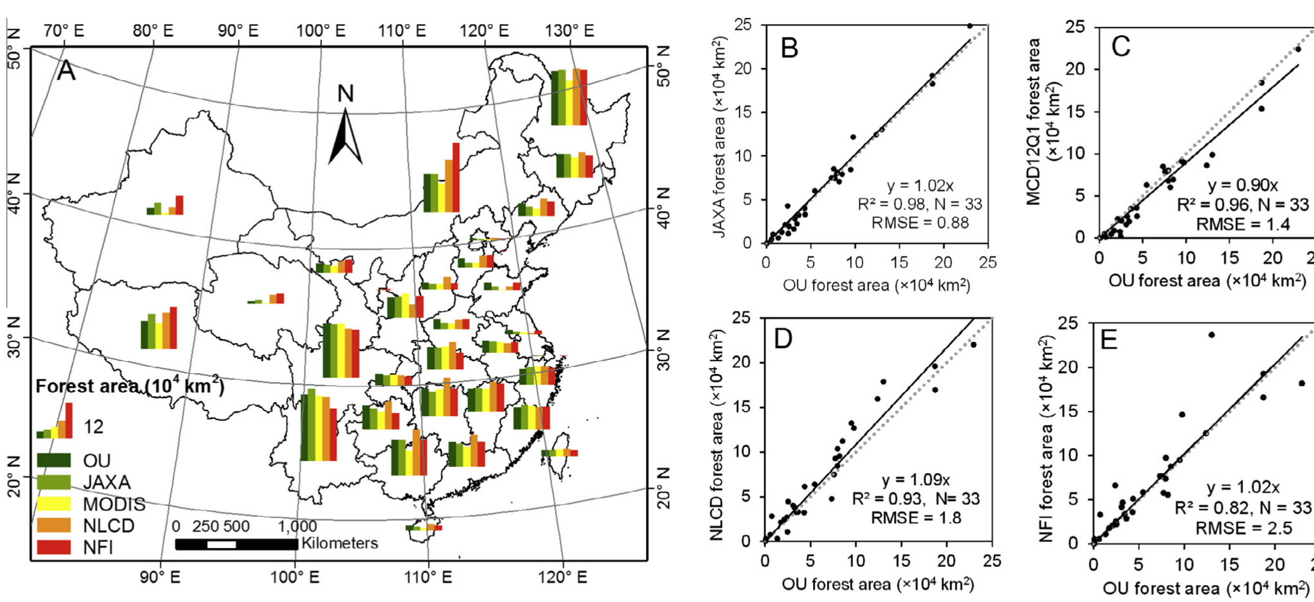


**Fig. 10.** Forest area comparison among multi-source forest datasets in provinces in China in 2010.

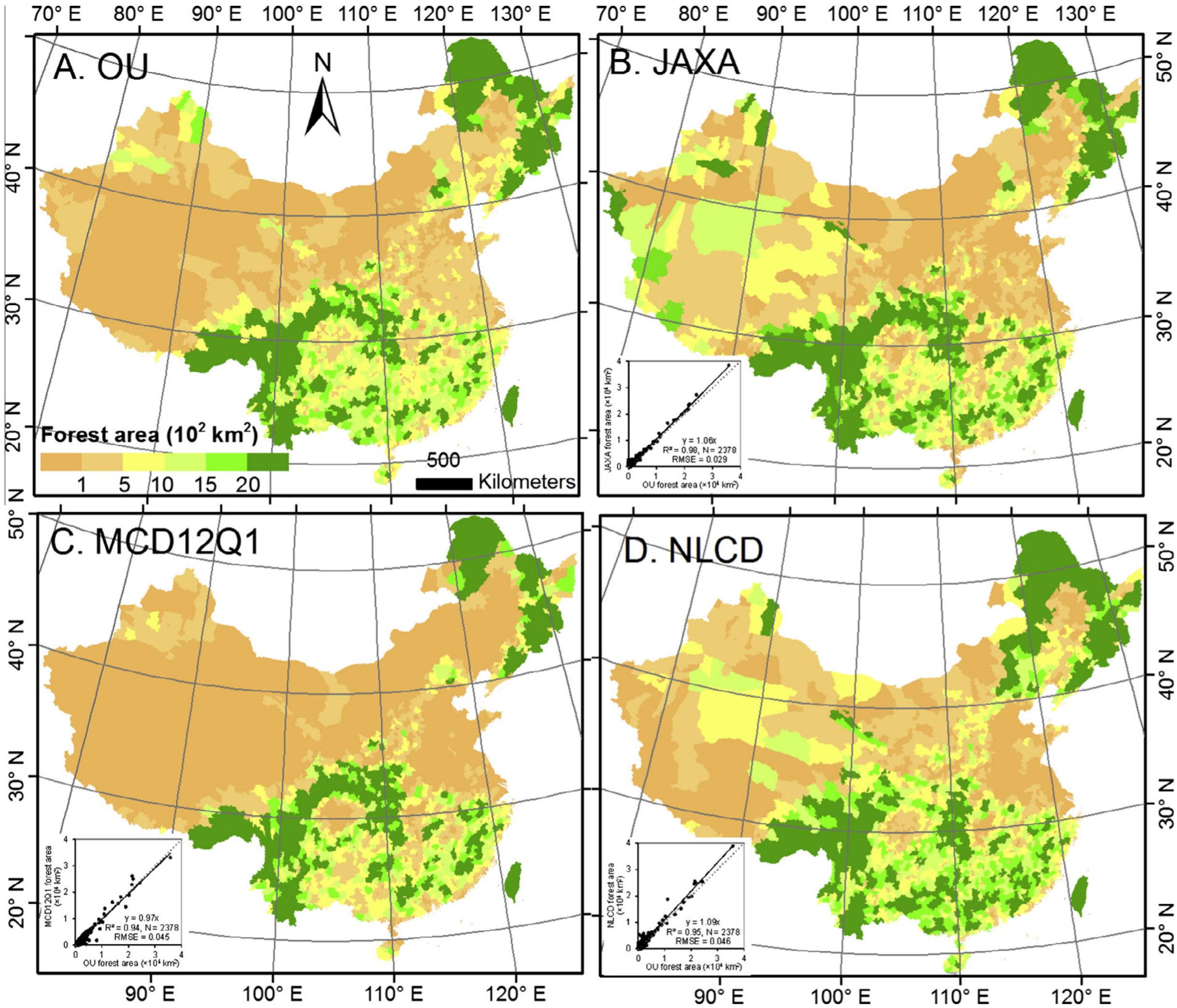


**Fig. 11.** Forest area comparison among multi-source forest datasets at counties in China in 2010.

China, in comparison with the NLCD-China F/NF map. Some relatively large differences between the OU and NLCD-China F/NF maps occur in Central and Southern China.

## 4. Discussion

### 4.1. PALSAR-based algorithm for forest mapping

The large uncertainty of multi-source forest maps and their changes affect our studies of climate dynamics, ecological services, and biodiversity. In this study, we developed a PALSAR-based algorithm for forest mapping at 50-m spatial resolution, based on the threshold value combination of HV, HH–HV, and HH/HV. Forest and non-forest can be easily distinguishable in HV images (Shimada et al., 2014), and the HV polarized images may be one of the best choices for forest mapping in mountainous areas as it was less sensitive to slope variations (Jensen, 2006). HH–HV and HH/HV were also included to exclude the commission errors from cropland and built-up lands. PALSAR images were proved to be stable from 2006 to 2010, as well as the gamma-naught of HH and HV for forest areas (Shimada et al., 2014). Although the threshold values are first derived from the ROIs in Mainland Southeast Asia in 2009 (Dong et al., 2012a), they are suitable for forest mapping in other years. Forests have similar backscatter signature contributed by similar physical structures, which would have small differences for different forest types, terrain and soil moisture (Shimada et al., 2014). It is estimated that approximately 92.4%, 94.1%, and 88.4% of forest ROIs pixels in China are in the threshold intervals of HV, HH/HV, and HH–HV (95% confidence level) in Mainland Southeast Asia, indicating the same threshold values can be extended to China for forest mapping (Fig. 14).

The JAXA F/NF map used the median filter in data analysis, which presents high accuracy in those areas with large forest patches, but may overestimate or underestimate the forest distribution in certain regions with small forest patches. The OU and JAXA F/NF maps present similar distribution histograms in HH, HV, Ratio, and Difference (Fig. 15). Approximately 26% of forests in JAXA F/NF map were out of the threshold interval in East Asia (Fig. 15B), which would be attributed to the median filter in the pre-processing and the algorithm. Compared with the JAXA F/NF map, several improvements are achieved in the OU F/NF map in China. First, we use the same threshold values to map forests in different climate regions from Mainland Southeast Asia to China. Second, the annual maximum NDVI mask effectively excludes the commissioned forests from mountains, barren lands, and sparely vegetated lands (Fig. 16A). Third, more forests are identified in the major agricultural production areas in China (Fig. 16B). Fourth, the detailed distribution of forest/non-forest pixels are preserved in this study (Fig. 16C).

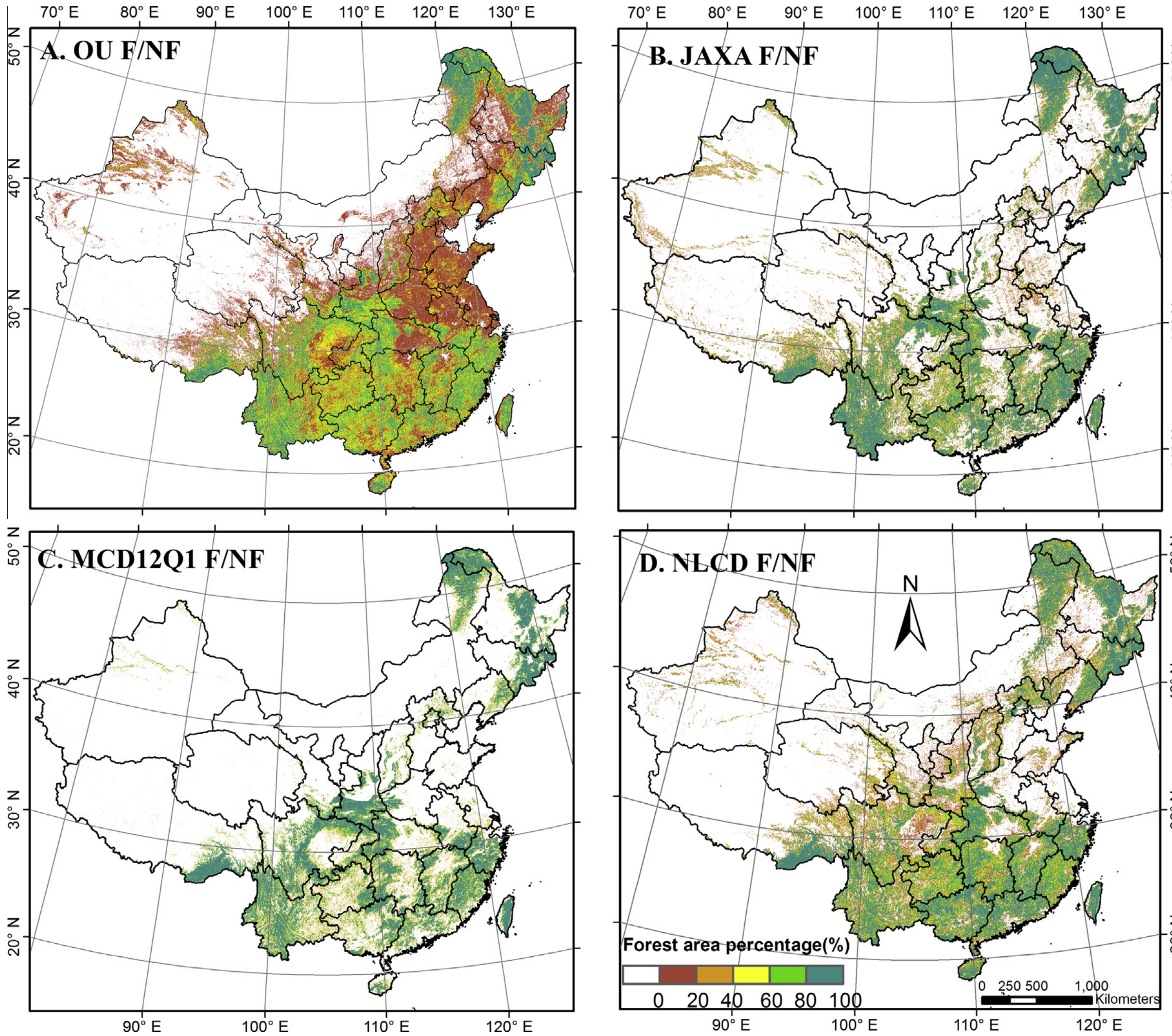


**Fig. 12.** Spatial distribution of forest/non-forest maps at 1 km spatial resolution in China in 2010: (A) OU F/NF, (B) JAXA F/NF, (C) MCD12Q1 F/NF, and (D) NLCD-China F/NF.

### *4.2. Factors for the differences among the multi-source forest maps in China*

Considering the features of multi-source forest datasets, three main factors might be responsible for their differences in area estimates and spatial distribution in China, including the definition of forests, data sources, and the algorithms for forest mapping.

(1) Definition of forests among the multi-source forest maps

The forests in the FAO FRA are defined as the land (0.5 ha) with tree crown cover more than 10% and a minimum tree height of 5-m (FAO, 2012). The JAXA (Shimada et al., 2014) and OU F/NF maps use similar definition of forests with the FAO FRA, which may explain why their forest area estimates are almost the same (Fig. 9). The forest definition in the NLCD-China dataset requires tree canopy cover more than 10%, but no criterion for tree height (Liu et al., 2005). The forests in the MCD12Q1 (IGBP) dataset are defined as the land dominated by woody vegetation covering more than 60% and tree height exceeding 2-m (Friedl et al., 2010). The forests in the NFI-China dataset are divided into natural, secondary, and planted forests, all of which have more than 30% coverage (Forestry Ministry of China, 1983).

(2) Data source

The FAO FRA and NFI-China forest datasets are primarily based on in-situ forest inventory data and statistics, with supplemental information from remote sensing, and have rich information such as forest species, stand age, and forest management. However, these datasets are only available at country or province scales. The reliability of the MCD12Q1 product would degrade with substantial levels of missing data because of heavy cloud cover, especially in the tropical regions, and low illumination and polar night in the northern high latitudes (Friedl et al., 2010). 30-m Landsat images have much finer spatial resolution than other primary satellite images. The high data quality and reasonable acquisition time of Landsat TM/ETM+ images are necessary for NLCD-China, as only one image is used for the interpretation and digitalization (Liu et al., 2005; Zhang et al., 2014). The backscatter signature of land cover types from PALSAR data can be used to distinguish forest and non-forest, but limited by the observation frequency, data acquisition time, soil moisture, and complex terrain (Figs. S4 and S5). The spatial resolution and acquisition date of PALSAR data used for OU and JAXA F/NF maps are different. 50-m PALSAR FBD data in the main growing season was used to generate OU F/NF map, while 25-m PALSAR FBD data from June to September was used to generate JAXA F/NF maps (Shimada et al., 2014).

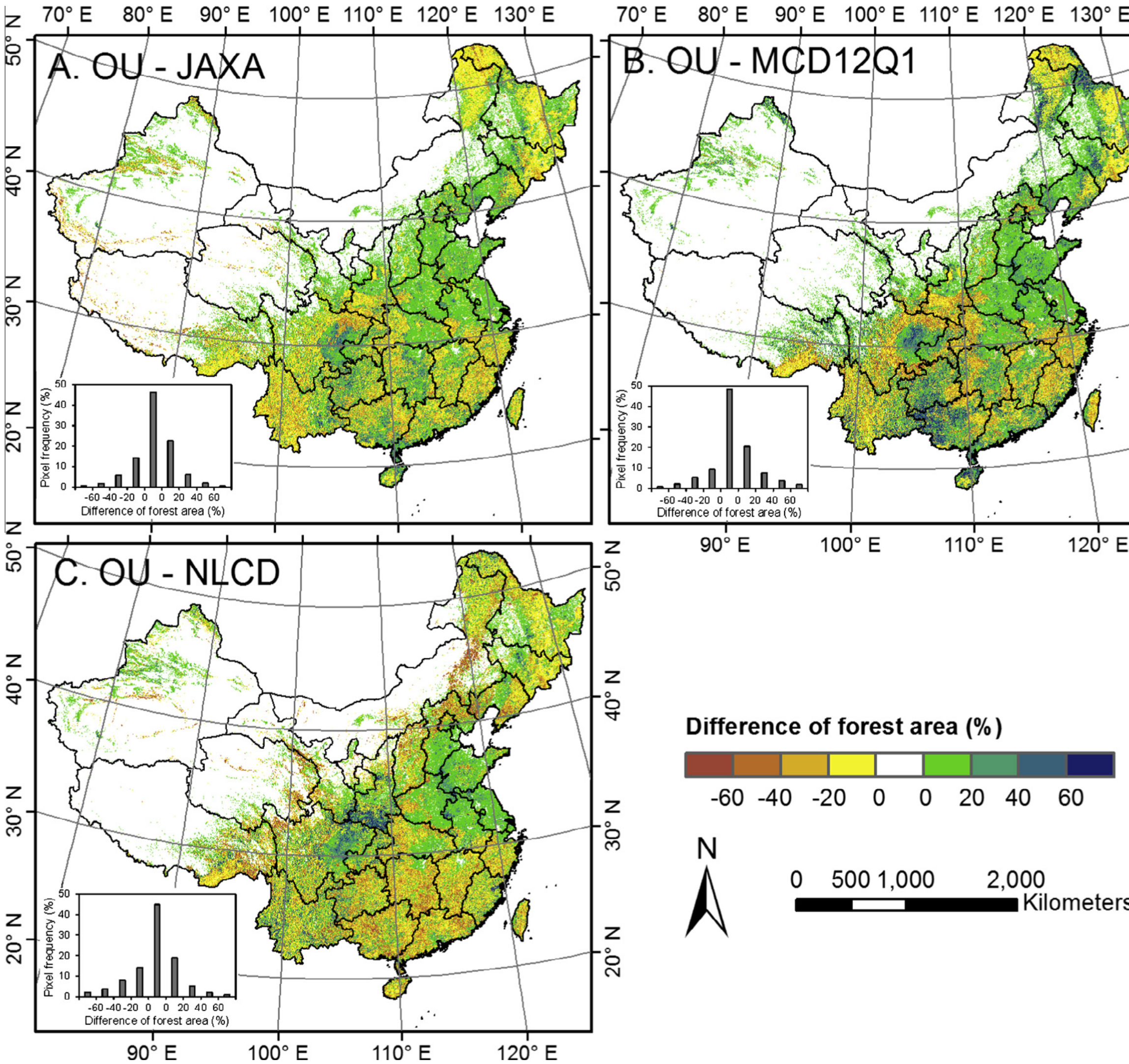


**Fig. 13.** Spatial distribution comparison among multi-source forest maps at the spatial resolution of 1 km in China in 2010. (A–C) Are the spatial comparison between OU F/NF and JAXA, MCD12Q1 and NLCD F/NF maps, respectively.

(3) Forest mapping algorithms

There are two general approaches to estimate forest area: (1) forest inventory and statistics, including the FAO FRA and NFI-China, and (2) remote sensing, including OU, JAXA, MCD12Q1, and NLCD-China F/NF maps. FAO FRA provides a simple way to estimate global and regional forest area and changes, based on the data from governments and research groups. A 5-year to 10-year period was usually needed to produce each NFI-China, as it consumes huge investment and labor force, compared with the other forest products. Intensive forest inventories have obtained a lot of forest samples in different countries for several decades (FAO, 2012). The NFI datasets are considered reliable and widely used to estimate forest area changes (Ohmann et al., 2014; Vibrans et al., 2013) and analyze their effects on carbon balance (Fang et al., 2014a, 2001, 2014b).

Human–computer interactive method, i.e. visual interpretation and digitalization on the screen, is used in the NLCD-China project. This procedure is time consuming and requires a large number of labor force. The accuracy depends on the knowledge and skill of different interpreters about the spectral and geometric features of different land cover types from Landsat images. Only the land cover change polygons larger than 4 ha were drawn when updating NLCD-China, so small change areas were missed. However, this method can work better than automated algorithms in comprehensive land cover classification and has obtained satisfactory results (Zhang et al., 2014).

The automated supervised classification algorithms, used by OU, JAXA, and MCD12Q1 F/NF maps, has high efficiency of processing large volume of satellite images to map land cover types. These algorithms work well for certain land cover types with homogenous spectral or backscatter features, but often perform not well in the areas with complex land cover types. Some pre-processing or post-processing are included to eliminate the image noises and improve the product accuracy, such as median filter, region segmentation, and spatial probability adjustment for mixed pixels.

### 4.3. Implication of this study

China has the fifth largest forest area (FAOSTAT, 2011) and the largest plantation forest area (State Forestry Bureau, 2014) in the world. The area of plantation forest accounts for approximately 36% of the total forest area in China. In the past 40 years, the forest area and volume have increased at the rates of 80% and 75%, respectively (State Forestry Bureau, 2014), indicating substantial carbon storage and sequestration by forests. Although more and more global and regional forest cover maps have become available,

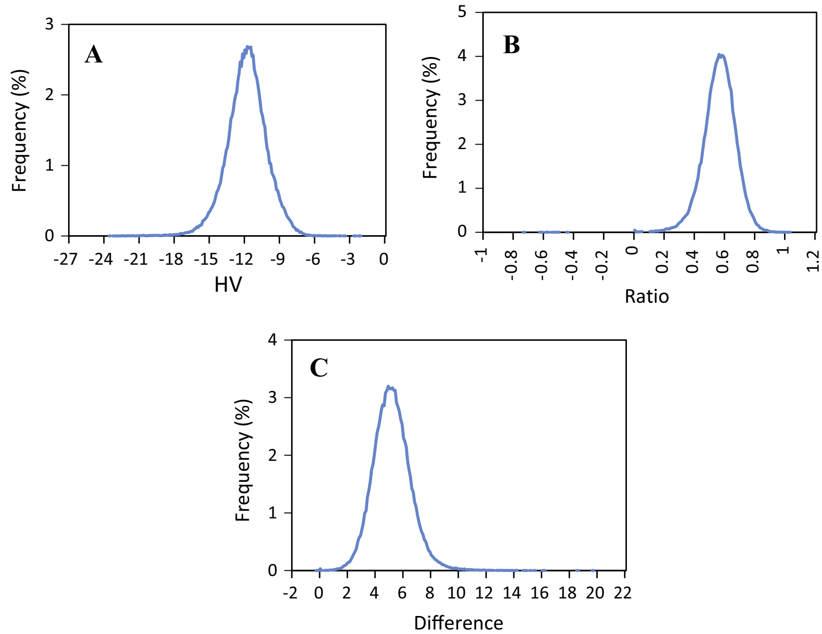


**Fig. 14.** The backscatter signatures of forest ROIs defined based on high spatial resolution images from Google Earth in China in circa 2010: (A) HV, (B) HH/HV, and (C) HH–HV.

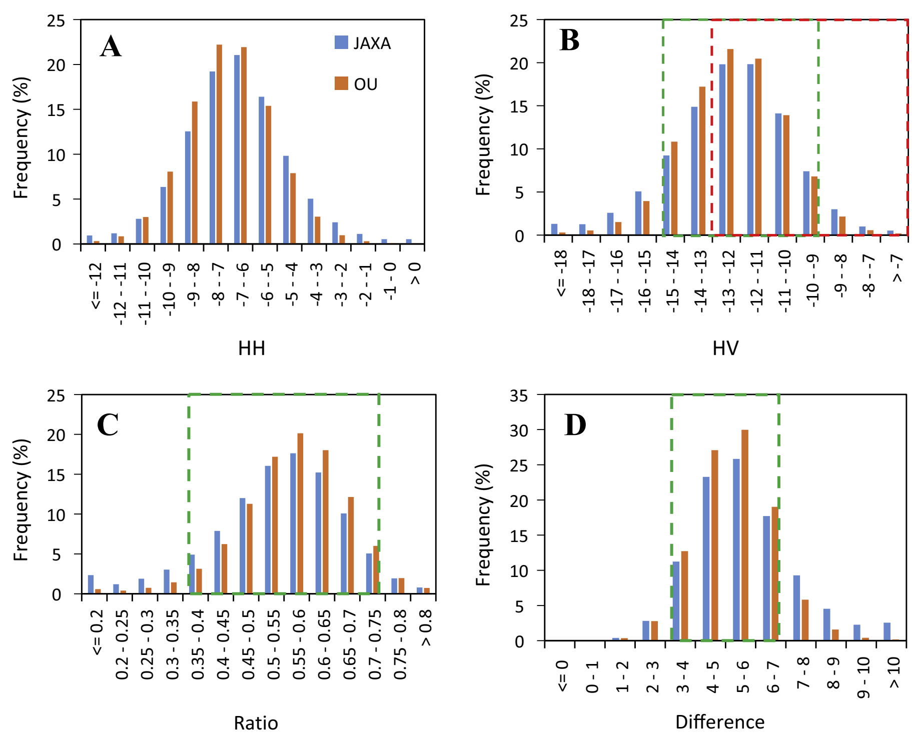


**Fig. 15.** The polarization signatures with forest pixels of OU F/NF map and JAXA F/NF map. The green and red rectangles represent the threshold values for forest mapping of OU F/NF map and JAXA F/NF map. (For interpretation of the references to color in this figure legend, the reader is referred to the web version of this article.)

some uncertainties about the area and distribution of forests and plantations still exist, especially in regions with large changes in forests. The PALSAR-based algorithm developed in this study can generate accurate and detailed forest maps at 50-m spatial resolution in a simple and robust way. The low forest area percentage within 1-km grid cells estimated by the OU F/NF map indicates large potential for further reforestation/afforestation and carbon sequestration in the future (Fig. 9). The PALSAR-based algorithm also provides a potential method to assess the reforestation/afforestation effects of various ecological restoration projects in China, such as Three-North Shelterbelt Program across the Northeast, North, and the Northwest of China from 1978 to 2050, and six super large forestry projects started in the early 21st century. The accurate distribution and dynamics of forests could serve as an important baseline data for carbon cycle, forest management and policy.

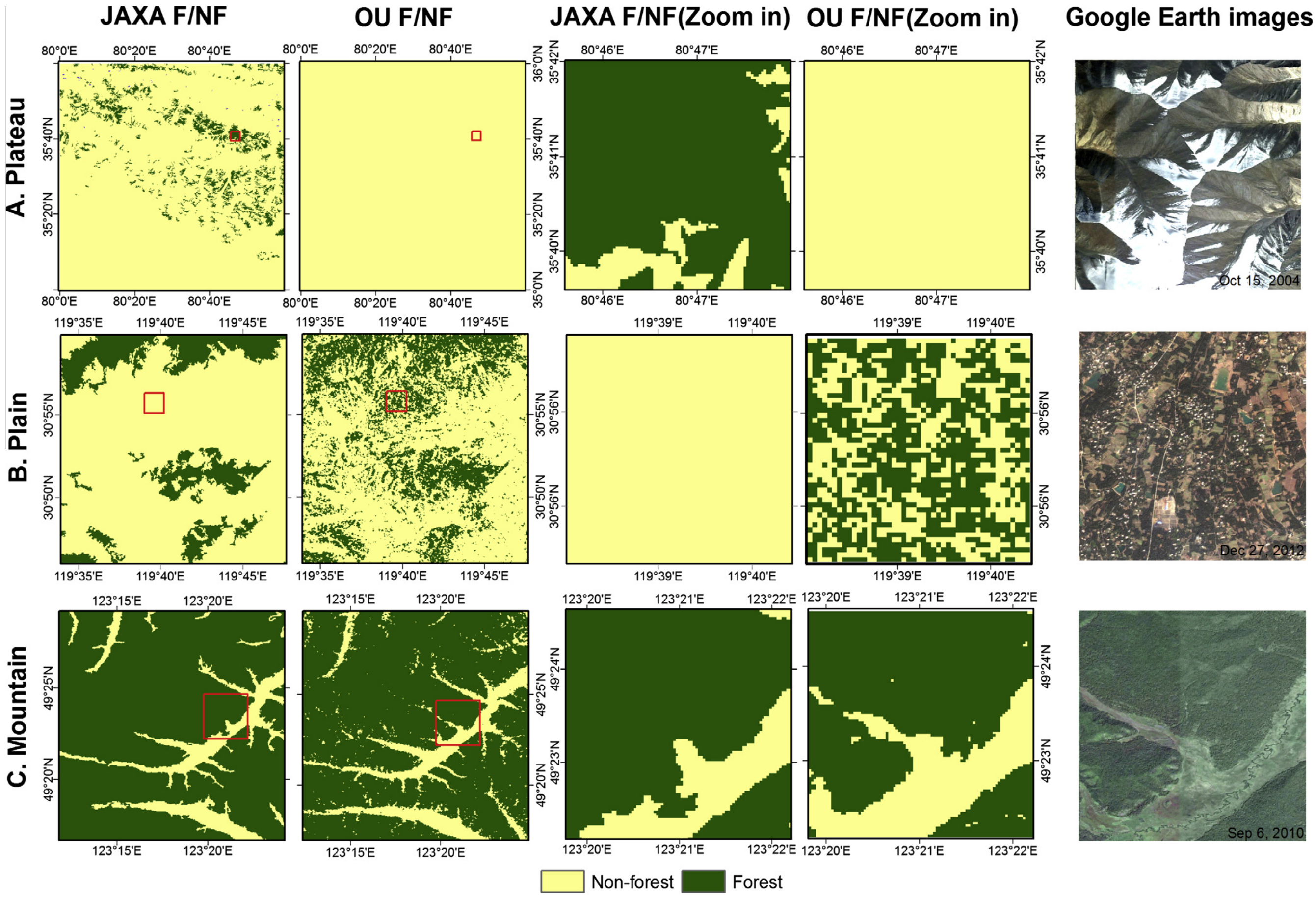


**Fig. 16.** Comparison between OU F/NF map and JAXA F/NF map in the plateau (A), plain (B), and mountain regions (C) in China in 2010.

In recent years, the Chinese government is paying great attention to the protection of natural forests, while the demand for timber in China is increasing, which results in a large gap for the supply and demand of forest products. An annual average of $3.1 \times 10^7$ m$^3$ crude wood is imported into China, in addition to other kinds of wood products (State Forestry Bureau, 2012). Under the financial benefit from the local government's subsidy and cash income, Poplar and other types of tree plantations expanded extensively in the major agricultural production area, especially in the North China Plain. These forests are mainly the household-based plantations and distributed in small-size patches over landscapes. The plantation forest encroachment into croplands could pose a threat to food production and food security in those regions with limited cropland area, which is now a growing concern in China. Until now, there is no detailed information about the agro-forests in China. The 50-m PALSAR-based algorithm in this study can identify these forests in the major agricultural production, which can be used to assess the effects of forest plantation expansion on food security and cropland quality.

## 5. Conclusion

Some uncertainty exists among multi-source forest cover maps and inventory-based forest datasets in China in 2010, which highlight the needs to produce an accurate forest map at fine spatial resolution (e.g., 50-m). An algorithm was developed to map the area and spatial distribution of forests, based on the combination of PALSAR FBD data and MODIS NDVI in 2010. The resultant 50-m PALSAR-based forest cover map was proved to be reasonably accurate, through the accuracy assessment of ground truth samples, with an overall accuracy of 96.2%, and comparison with JAXA, MCD12Q1, NLCD-China, FAO FRA, and NFI-China F/NF datasets. Large areas of forests, in the major grain production plains with the elevation lower than 200 m, were identified in the OU F/NF map, compared with the other forest/non-forest datasets. The resultant map of forests in China, together with the forest maps in Southeast Asia (Dong et al., 2012a), have demonstrated that the PALSAR-based algorithm developed could be applied to map forests in the whole monsoon Asia where forests may have similar physical structure and backscatter signature. The resultant 50-m forest cover map can serve as a background map to investigate forest changes and their effects on carbon cycle, food security and ecosystem services.

## Acknowledgements

This study was supported in part by the research grants from the National Aeronautics and Space Administration (NASA) Land Cover and Land Use Change program (NNX11AJ35G and NNX14AD78G), the US National Science Foundation (NSF) EPSCoR program (IIA-1301789), and the National Institutes of Health (NIH) NIAID (1R01AI101028-01A1). We thank Sarah Xiao for English editing of the manuscript.

## Appendix A. Supplementary material

Supplementary data associated with this article can be found, in the online version, at http://dx.doi.org/10.1016/j.isprsjprs.2015.08.010.

## References


Achard, F., Hansen, M.C., 2012. Global Forest Monitoring from Earth Observation. CRC Press.

Bagan, H., Kinoshita, T., Yamagata, Y., 2012. Combination of AVNIR-2, PALSAR, and polarimetric parameters for land cover classification. IEEE Trans. Geosci. Remote Sens. 50, 1318–1328.

Ban, Y.F., Hu, H.T., Rangel, I.M., 2010. Fusion of Quickbird MS and RADARSAT SAR data for urban land-cover mapping: object-based and knowledge-based approach. Int. J. Remote Sens. 31, 1391–1410.

Bartholome, E., Belward, A.S., 2005. GLC2000: a new approach to global land cover mapping from earth observation data. Int. J. Remote Sens. 26, 1959–1977.

Bonan, G.B., 2008. Forests and climate change: forcings, feedbacks, and the climate benefits of forests. Science 320, 1444–1449.

Bontemps, S., Defourny, P., Bogaert, E.V., Arino, O., Kalogirou, V., Perez, J.R., 2011. GLOBCOVER 2009 Products Description and Validation Report.

Defries, R.S., Townshend, J.R.G., 1994. Ndvi-derived land-cover classifications at a global-scale. Int. J. Remote Sens. 15, 3567–3586.

Dong, J.W., Xiao, X.M., Chen, B.Q., Torbick, N., Jin, C., Zhang, G.L., Biradar, C., 2013. Mapping deciduous rubber plantations through integration of PALSAR and multi-temporal Landsat imagery. Remote Sens. Environ. 134, 392–402.

Dong, J.W., Xiao, X.M., Sheldon, S., Biradar, C., Duong, N.D., Hazarika, M., 2012a. A comparison of forest cover maps in Mainland Southeast Asia from multiple sources: PALSAR, MERIS, MODIS and FRA. Remote Sens. Environ. 127, 60–73.

Dong, J.W., Xiao, X.M., Sheldon, S., Biradar, C., Xie, G.S., 2012b. Mapping tropical forests and rubber plantations in complex landscapes by integrating PALSAR and MODIS imagery. ISPRS J. Photogramm. Remote Sens. 74, 20–33.

Dong, J.W., Xiao, X.M., Sheldon, S., Biradar, C., Zhang, G.L., Duong, N.D., Hazarika, M., Wikantika, K., Takeuhci, W., Moore, B., 2014. A 50-m forest cover map in Southeast Asia from ALOS/PALSAR and its application on forest fragmentation assessment. PLoS One 9.

Fang, J., Kato, T., Guo, Z., Yang, Y., Hu, H., Shen, H., Zhao, X., Kishimoto-Mo, A.W., Tang, Y., Houghton, R.A., 2014a. Evidence for environmentally enhanced forest growth. Proc. Natl. Acad. Sci. USA 111, 9527–9532.

Fang, J.Y., Chen, A.P., Peng, C.H., Zhao, S.Q., Ci, L., 2001. Changes in forest biomass carbon storage in China between 1949 and 1998. Science 292, 2320–2322.

Fang, J.Y., Guo, Z.D., Hu, H.F., Kato, T., Muraoka, H., Son, Y., 2014b. Forest biomass carbon sinks in East Asia, with special reference to the relative contributions of forest expansion and forest growth. Global Change Biol. 20, 2019–2030.

FAO, 2009. How to Feed the World in 2050. Rome.

FAO, 2012. Forest Resource Assessment (FRA) 2010. Rome.

FAOSTAT, 2011. <http://faostat.fao.org/>.

Foley, J.A., DeFries, R., Asner, G.P., Barford, C., Bonan, G., Carpenter, S.R., Chapin, F.S., Coe, M.T., Daily, G.C., Gibbs, H.K., Helkowski, J.H., Holloway, T., Howard, E.A., Kucharik, C.J., Monfreda, C., Patz, J.A., Prentice, I.C., Ramankutty, N., Snyder, P.K., 2005. Global consequences of land use. Science 309, 570–574.

Forestry Ministry of China, 1983. Technical Standards for Forest Resource Measurement. China Forestry Publishing Press, Beijing.

Friedl, M.A., Sulla-Menashe, D., Tan, B., Schneider, A., Ramankutty, N., Sibley, A., Huang, X.M., 2010. MODIS collection 5 global land cover: algorithm refinements and characterization of new datasets. Remote Sens. Environ. 114, 168–182.

Gibbs, H.K., Ruesch, A.S., Achard, F., Clayton, M.K., Holmgren, P., Ramankutty, N., Foley, J.A., 2010. Tropical forests were the primary sources of new agricultural land in the 1980s and 1990s. Proc. Natl. Acad. Sci. USA 107, 16732–16737.

Giri, C., Ochieng, E., Tieszen, L.L., Zhu, Z., Singh, A., Loveland, T., Masek, J., Duke, N., 2011. Status and distribution of mangrove forests of the world using earth observation satellite data. Global Ecol. Biogeogr. 20, 154–159.

Gong, P., Wang, J., Yu, L., Zhao, Y.C., Zhao, Y.Y., Liang, L., Niu, Z.G., Huang, X.M., Fu, H. H., Liu, S., Li, C.C., Li, X.Y., Fu, W., Liu, C.X., Xu, Y., Wang, X.Y., Cheng, Q., Hu, L.Y., Yao, W.B., Zhang, H., Zhu, P., Zhao, Z.Y., Zhang, H.Y., Zheng, Y.M., Ji, L.Y., Zhang, Y. W., Chen, H., Yan, A., Guo, J.H., Yu, L., Wang, L., Liu, X.J., Shi, T.T., Zhu, M.H., Chen, Y.L., Yang, G.W., Tang, P., Xu, B., Giri, C., Clinton, N., Zhu, Z.L., Chen, J., Chen, J., 2013. Finer resolution observation and monitoring of global land cover: first mapping results with Landsat TM and ETM+ data. Int. J. Remote Sens. 34, 2607–2654.

Groombridge, B., Jenkins, M.D., 2002. World Atlas of Biodiversity. University of California Press, Berkeley.

Hansen, M.C., Defries, R.S., Townshend, J.R.G., Sohlberg, R., 2000. Global land cover classification at 1 km spatial resolution using a classification tree approach. Int. J. Remote Sens. 21, 1331–1364.

Hansen, M.C., Potapov, P.V., Moore, R., Hancher, M., Turubanova, S.A., Tyukavina, A., Thau, D., Stehman, S.V., Goetz, S.J., Loveland, T.R., Kommareddy, A., Egorov, A., Chini, L., Justice, C.O., Townshend, J.R.G., 2013. High-resolution global maps of 21st-century forest cover change. Science 342, 850–853.

Hansen, M.C., Stehman, S.V., Potapov, P.V., Loveland, T.R., Townshend, J.R.G., DeFries, R.S., Pittman, K.W., Arunarwati, B., Stolle, F., Steininger, M.K., Carroll, M., DiMiceli, C., 2008. Humid tropical forest clearing from 2000 to 2005 quantified by using multitemporal and multiresolution remotely sensed data. Proc. Natl. Acad. Sci. USA 105, 9439–9444.

Hoan, N.T., Tateishi, R., Alsaaideh, B., Ngigi, T., Alimuddin, I., Johnson, B., 2013. Tropical forest mapping using a combination of optical and microwave data of ALOS. Int. J. Remote Sens. 34, 139–153.

Imhoff, M.L., 1995. A theoretical-analysis of the effect of forest structure on synthetic-aperture radar backscatter and the remote-sensing of biomass. IEEE Trans. Geosci. Remote Sens. 33, 341–352.

Jensen, J.R., 2006. Remote Sensing of the Environment: An Earth Resource Perspective, second ed. Prentice Hall.

Kovacs, J.M., Lu, X.X., Flores-Verdugo, F., Zhang, C., de Santiago, F.F., Jiao, X., 2013. Applications of ALOS PALSAR for monitoring biophysical parameters of a degraded black mangrove (*Avicennia germinans*) forest. ISPRS J. Photogramm. Remote Sens. 82, 102–111.

Lambin, E.F., Meyfroidt, P., 2011. Global land use change, economic globalization, and the looming land scarcity. Proc. Natl. Acad. Sci. USA 108, 3465–3472.

Lehmann, E.A., Caccetta, P.A., Zhou, Z.S., McNeill, S.J., Wu, X.L., Mitchell, A.L., 2012. Joint processing of Landsat and ALOS-PALSAR data for forest mapping and monitoring. IEEE Trans. Geosci. Remote Sens. 50, 55–67.

Leinenkugel, P., Esch, T., Kuenzer, C., 2011. Settlement detection and impervious surface estimation in the Mekong Delta using optical and SAR remote sensing data. Remote Sens. Environ. 115, 3007–3019.

Liu, D., Chen, Y., Cai, W.W., Dong, W.J., Xiao, J.F., Chen, J.Q., Zhang, H.C., Xia, J.Z., Yuan, W.P., 2014. The contribution of China's Grain to Green Program to carbon sequestration. Landscape Ecol. 29, 1675–1688.

Liu, J.Y., Liu, M.L., Tian, H.Q., Zhuang, D.F., Zhang, Z.X., Zhang, W., Tang, X.M., Deng, X. Z., 2005. Spatial and temporal patterns of China's cropland during 1990–2000: an analysis based on Landsat TM data. Remote Sens. Environ. 98, 442–456.

Longepe, N., Rakwatin, P., Isoguchi, O., Shimada, M., Uryu, Y., Yulianto, K., 2011. Assessment of ALOS PALSAR 50 m orthorectified FBD data for regional land cover classification by support vector machines. IEEE Trans. Geosci. Remote Sens. 49, 2135–2150.

Loveland, T.R., Reed, B.C., Brown, J.F., Ohlen, D.O., Zhu, Z., Yang, L., Merchant, J.W., 2000. Development of a global land cover characteristics database and IGBP DISCover from 1 km AVHRR data. Int. J. Remote Sens. 21, 1303–1330.

Motohka, T., Shimada, M., Uryu, Y., Setiabudi, B., 2014. Using time series PALSAR gamma nought mosaics for automatic detection of tropical deforestation: a test study in Riau, Indonesia. Remote Sens. Environ. 155, 79–88.

Ni, W.J., Sun, G.Q., Guo, Z.F., Zhang, Z.Y., He, Y.T., Huang, W.L., 2013. Retrieval of forest biomass from ALOS PALSAR data using a lookup table method. IEEE J. Sel. Top. Appl. Earth Observ. Remote Sens. 6, 875–886.

Ohmann, J.L., Gregory, M.J., Roberts, H.M., 2014. Scale considerations for integrating forest inventory plot data and satellite image data for regional forest mapping. Remote Sens. Environ. 151, 3–15.

Pan, Y.D., Birdsey, R.A., Fang, J.Y., Houghton, R., Kauppi, P.E., Kurz, W.A., Phillips, O.L., Shvidenko, A., Lewis, S.L., Canadell, J.G., Ciais, P., Jackson, R.B., Pacala, S.W., McGuire, A.D., Piao, S.L., Rautiainen, A., Sitch, S., Hayes, D., 2011. A large and persistent carbon sink in the world's forests. Science 333, 988–993.

Pantze, A., Santoro, M., Fransson, J.E.S., 2014. Change detection of boreal forest using bi-temporal ALOS PALSAR backscatter data. Remote Sens. Environ. 155, 120–128

Peregon, A., Yamagata, Y., 2013. The use of ALOS/PALSAR backscatter to estimate above-ground forest biomass: a case study in Western Siberia. Remote Sens. Environ. 137, 139–146.

Pongratz, J., Reick, C.H., Raddatz, T., Claussen, M., 2010. Biogeophysical versus biogeochemical climate response to historical anthropogenic land cover change. Geophys. Res. Lett. 37.

Potapov, P., Turubanova, S., Hansen, M.C., 2011. Regional-scale boreal forest cover and change mapping using Landsat data composites for European Russia. Remote Sens. Environ. 115, 548–561.

Rakwatin, P., Longepe, N., Isoguchi, O., Shimada, M., Uryu, Y., Takeuchi, W., 2012. Using multiscale texture information from ALOS PALSAR to map tropical forest. Int. J. Remote Sens. 33, 7727–7746.

Rosenqvist, A., Shimada, M., Chapman, B., Freeman, A., De Grandi, G., Saatchi, S., Rauste, Y., 2000. The Global Rain Forest Mapping project – a review. Int. J. Remote Sens. 21, 1375–1387.

Sheldon, S., Xiao, X.M., Biradar, C., 2012. Mapping evergreen forests in the Brazilian Amazon using MODIS and PALSAR 500-m mosaic imagery. ISPRS J. Photogramm. Remote Sens. 74, 34–40.

Shimada, M., 2005. Long-term stability of L-band normalized radar cross section of Amazon rainforest using the JERS-1 SAR. Can. J. Remote Sens. 31, 132–137.

Shimada, M., Isoguchi, O., Tadono, T., Isono, K., 2009. PALSAR radiometric and geometric calibration. IEEE Trans. Geosci. Remote Sens. 47, 3915–3932.

Shimada, M., Itoh, T., Motooka, T., Watanabe, M., Shiraishi, T., Thapa, R., Lucas, R., 2014. New global forest/non-forest maps from ALOS PALSAR data (2007–2010). Remote Sens. Environ. 155, 13–31.

Shimada, M., Ohtaki, T., 2010. Generating large-scale high-quality SAR mosaic datasets: application to PALSAR data for global monitoring. IEEE J. Sel. Top. Appl. Earth Observ. Remote Sens. 3, 637–656.

Solano, R., Didan, K., Jacobson, A., Huete, A., 2010. MODIS Vegetation Index User's Guide (MOD13 Series). Vegetation Index and Phenology Lab, The University of Arizona.

State Forestry Bureau, 2003. Technical Regulation for National Forestry Inventory.

State Forestry Bureau, 2012. China Forestry Statistical Yearbook. China Forestry Publishing House.

State Forestry Bureau, 2014. Brief Introduction of Forest Resources in China––The Eighth National Forestry Inventory.

Vibrans, A.C., McRoberts, R.E., Moser, P., Nicoletti, A.L., 2013. Using satellite image-based maps and ground inventory data to estimate the area of the remaining Atlantic forest in the Brazilian state of Santa Catarina. Remote Sens. Environ. 130, 87–95.

Xiao, J.F., 2014. Satellite evidence for significant biophysical consequences of the "Grain for Green" Program on the Loess Plateau in China. J. Geophys. Res.-Biogeosci. 119, 2261–2275.

Yu, G., Chen, Z., Piao, S., Peng, C., Ciais, P., Wang, Q., Li, X., Zhu, X., 2014. High carbon dioxide uptake by subtropical forest ecosystems in the East Asian monsoon region. Proc. Natl. Acad. Sci. USA 111, 4910–4915.

Zhang, Z., 2012. Remote Sensing Monitoring of Land Use in China. Starmap, Beijing.

Zhang, Z., Wang, X., Zhao, X., Liu, B., Yi, L., Zuo, L., Wen, Q., Liu, F., Xu, J., Hu, S., 2014. A 2010 update of National Land Use/Cover Database of China at 1:100,000 scale using medium spatial resolution satellite images. Remote Sens. Environ. 149, 142–154.